6 Glacier Thermodynamics

6.1 CONSERVATION OF ENERGY

The temperature distribution in a glacier is important because the rate of deformation increases rapidly as the ice becomes warmer (Section 2.2). Further, where the basal temperature reaches the pressure-melting temperature, basal melting may lead to the development of an interstitial layer of meltwater and the onset of basal sliding, resulting in ice velocities that can be orders of magnitude greater than those associated with internal deformation (c.f. Chapter 7). The starting point when considering the heat budget of a glacier is the first law of thermodynamics, which states that, in a closed system, no energy can be created or destroyed. Using this law, and some elementary thermodynamics, the thermodynamic or temperature equation can be derived. The following discussion is largely based on the extensive treatment of this topic given in Brown (1991). Readers not interested in the nuts and bolts of thermodynamics can skip this section and take equation (6.17) for granted.

The first law of thermodynamics may be reworded to say that the change in internal energy, dE, of a closed system with a given volume must be equal to the sum of the work done on the system, dW, and heat added to the volume, dQ. Thus, the rate of change of internal energy is given by

$$\frac{dE}{dt} = \frac{dW}{dt} + \frac{dQ}{dt}. \tag{6.1}$$

In glaciers, work energy is associated with the production of deformational heat, while Q represents heat released into the ice volume by conductive heat fluxes.

The kinetic energy of glaciers may be neglected, and the internal energy represents the thermal energy, which is related to the temperature of the ice. Defining the specific internal energy, e, as the thermal energy per unit mass, the rate of change in E can be written as

$$\frac{dE}{dt} = \frac{d(\rho e)}{dt} =$$

$$= \rho\frac{de}{dt} + e\frac{d\rho}{dt}, \tag{6.2}$$

where ρ represents the density of the ice. For an incompressible fluid, there is no transfer between internal energy and pressure, and

$$e = C_p T, \tag{6.3}$$

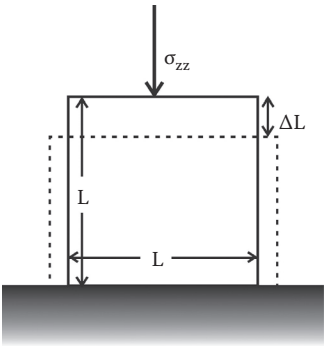

FIGURE 6.1 Deformation of a cube (L × L × L) under uniaxial compression.

with C_p the specific heat capacity and T the temperature. The specific heat capacity is the amount of energy needed to raise the temperature of a unit mass of ice by 1°C (or 1 K), under constant pressure. Further, for an incompressible material, the density may be considered constant, so that the second term on the right-hand side of equation (6.2) can be neglected and the change in internal energy is related to the temperature change as

$$\frac{dE}{dt} = \rho C_p \frac{dT}{dt}. \tag{6.4}$$

Work done on the system is associated with internal deformation of the ice. Assuming that no energy is expended toward mineralogical changes (for example, recrystallization), the work done can be found by considering deformation of a volume of ice (c.f. Means, 1976, pp. 266–267). Referring to Figure 6.1, consider a cube subject to a compressive stress, σ_{zz}. This stress causes the volume to shorten by a small amount ΔL. Recalling the definition of strain as the change in length per unit of original length, the change in length can be written as

$$\Delta L = \varepsilon_{zz} L. \tag{6.5}$$

With work defined as the product of force and displacement, the work done on the cube equals the total force acting on the cube multiplied by the change in length. Thus,

$$W = (\sigma_{zz} L^2)(\varepsilon_{zz} L). \tag{6.6}$$

Dividing by the volume of the cube gives the work per unit volume,

$$W_o = \sigma_{zz} \varepsilon_{zz}. \tag{6.7}$$

Differentiating with respect to time gives the rate of deformational heat production,

$$\frac{dW_o}{dt} = \dot{W}_o = \sigma_{zz} \dot{\varepsilon}_{zz}. \tag{6.8}$$

Similar expressions apply to work done by other stresses, and the total rate of heating is

$$\dot{W}_d = \dot{\varepsilon}_{ij}\,\sigma_{ij}, \tag{6.9}$$

using the summation convention over repeat indices.

In addition, heat may be added by freezing of meltwater. If the amount of meltwater that refreezes per unit time and volume is M_f, release of latent heat equals

$$\dot{W}_L = L_f\,M_f, \tag{6.10}$$

where L_f represents the specific latent heat of fusion.

The conductive heat flux in the ice, $\vec{F}_c$, is linked to the temperature gradient according to Fourier's law for heat conduction

$$\vec{F}_c = -k\nabla T, \tag{6.11}$$

where k denotes the thermal conductivity. The amount of heat released by this flux in a volume V enclosed by the closed surface A equals the total heat flux through the enclosing surface, A, and

$$\int_V \frac{dQ}{dt}\,dV = -\iint_A \vec{F}_c \bullet \vec{n}\,dA. \tag{6.12}$$

Here $\vec{n}$ represents the unit vector perpendicular to the enclosing surface, A. Applying Gauss's theorem to rewrite the surface integral on the right-hand side of equation (6.12) as a volume integral gives

$$\begin{aligned}\int_V \frac{dQ}{dt}\,dV &= \int_V \mathrm{div}\bullet\vec{F}_c\,dV = \\ &= k\int_V \nabla^2 T\,dV.\end{aligned} \tag{6.13}$$

Per unit volume, heating from conductive heat fluxes is then

$$\frac{dQ}{dt} = k\nabla^2 T. \tag{6.14}$$

The thermodynamic equation (6.1) can now be written as a temperature equation. Expression (6.4) links the internal energy to the temperature, while the heating terms are given by equations (6.9), (6.10), and (6.14). The result is

$$\rho C_p \frac{dT}{dt} = k\nabla^2 T + \dot{\varepsilon}_{ij}\,\sigma_{ij} + L_f\,M_f. \tag{6.15}$$

The time derivative on the left-hand side represents the total derivative and can be written as the sum of the local time change in temperature and advective changes associated with a spatially nonuniform temperature distribution. That is,

$$\frac{dT}{dt} \equiv \frac{\partial T}{\partial t} + \vec{u} \bullet \nabla T, \tag{6.16}$$

in which $\vec{u} = (u, v, w)$ represents the three-dimensional velocity vector. Written out in full, conservation of heat can now be expressed as

$$\begin{aligned}\frac{\partial T}{\partial t} = &- u\frac{\partial T}{\partial x} - v\frac{\partial T}{\partial y} - w\frac{\partial T}{\partial z} + \\ &+ K\frac{\partial^2 T}{\partial x^2} + K\frac{\partial^2 T}{\partial y^2} + K\frac{\partial^2 T}{\partial z^2} + \\ &+ \frac{1}{\rho C_p}(\dot{\varepsilon}_{xx}\sigma_{xx} + \dot{\varepsilon}_{yy}\sigma_{yy} + \dot{\varepsilon}_{zz}\sigma_{zz} + 2\dot{\varepsilon}_{xy}\sigma_{xy} + 2\dot{\varepsilon}_{xz}\sigma_{xz} + 2\dot{\varepsilon}_{yz}\sigma_{yz}) + \\ &+ \frac{L_f M_f}{\rho C_p}.\end{aligned} \tag{6.17}$$

In this equation, $K = k/(\rho C_p)$ represents the thermal diffusivity.

To recapitulate the foregoing, for incompressible ice with constant density, ρ, conservation of energy can be expressed in terms of change in temperature of the ice as done in equation (6.17). This temperature may change as a result of advection of heat (first line), diffusion of heat (second line), heat generated by internal deformation (third line), and latent heat released by refreezing meltwater (last line). Except where noted explicitly, the thermal parameters are considered constants, with values given in Table 6.1.

TABLE 6.1
Values of Thermal Parameters of Pure Ice at 0°C

Specific heat capacity	C_p	2097 J $kg^{-1}K^{-1}$
Specific latent heat of fusion	L_f	333.5 kJ kg^{-1}
Thermal conductivity	k	2.10 $Wm^{-1}K^{-1}$
Thermal diffusivity	K	$1.09 \cdot 10^{-6}$ m^2s^{-1}
		34.4 m^2yr^{-1}
Density	ρ	917 kg m^{-3}

Source: Yen, Y.-C., CRREL Report 81–10, Cold Regions Research and Engineering Laboratory, Hanover, NH, 27 pp., 1981.

In general, equation (6.17) cannot be solved analytically. Further, to be fully correct, the thermodynamic equation must be solved simultaneously with the velocity distribution because the two are coupled through the temperature dependence of the rate factor in the constitutive relation. However, by making some simplifying assumptions, the basic characteristics of the temperature distribution in glaciers can be investigated.

6.2 STEADY-STATE TEMPERATURE PROFILES

The first of only a handful of analytical solutions of the temperature equation was derived by Robin (1955). He made the following assumptions:

1. The basal temperature is below the pressure-melting temperature; thus the solution only applies to cold glaciers, frozen to their bed.
2. Horizontal diffusion of heat is much smaller than vertical diffusion; in most parts of a glacier, horizontal temperature gradients are much smaller than vertical gradients, so this assumption is probably valid for most glaciers.
3. Horizontal advection of heat is neglected; this is only true where the horizontal components of velocity are small, that is, near the divide of an ice sheet.
4. Heat generation from internal deformation may be taken into account by increasing the geothermal heat flux at the base of the glacier; because in a glacier frozen to its bed, vertical shear is largest in the lower layers (Figure 4.2), where the shear stress is largest, this assumption is a reasonable first approximation.

Under these assumptions, the temperature equation (6.17) reduces to

$$\frac{\partial T}{\partial t} = K\frac{\partial^2 T}{\partial z^2} - w\frac{\partial T}{\partial z}. \tag{6.18}$$

The first term on the right-hand side represents redistribution of heat through (molecular) diffusion, while the second term describes redistribution of heat by downward ice flow (advection).

To solve equation (6.18) analytically, two more assumptions are needed, namely

5. The ice sheet is in thermal steady state with $\partial T/\partial t = 0$.
6. The ice-sheet profile is also in steady state (otherwise the temperature would not be steady), and the vertical velocity can be simply linked to the accumulation rate; at the surface, the vertical velocity must balance accumulation, while at the base, the vertical velocity must be zero.

The simplest profile that satisfies assumption 6 is

$$w(z) = -\frac{Mz}{H}, \tag{6.19}$$

where M represents the surface mass balance expressed in meters of ice per year (M > 0 for accumulation). As shown in Figure 4.2, for lamellar flow the vertical velocity decreases almost linearly with depth in the upper 80% of the ice thickness. Near the base, the vertical velocity decreases more rapidly to zero at the bed. Thus, the profile (6.19) adopted by Robin (1955) may be expected to overestimate downward heat advection in the upper portion of the glacier.

The steady-state temperature can now be found by solving the simplified heat equation

$$K\frac{\partial^2 T}{\partial z^2} + \frac{Mz}{H}\frac{\partial T}{\partial z} = 0. \tag{6.20}$$

To find a solution, two boundary conditions are needed. At the surface, the temperature equals the prescribed surface temperature, T_s. At the base of the glacier, the vertical temperature gradient must match the geothermal heat flux, corrected if necessary to account for heat generated by internal deformation. Denoting the basal heat flux by G, the basal temperature gradient is

$$\left(\frac{\partial T}{\partial z}\right)_b = -\frac{G}{k}. \tag{6.21}$$

Invoking these two boundary conditions, integrating equation (6.20) twice with respect to z gives the temperature profile

$$T(z) - T_s = -\frac{G}{k}\int_0^z \exp(-\bar{z}^2 q^2)\, d\bar{z}, \tag{6.22}$$

with

$$q^2 = \frac{M}{2KH}. \tag{6.23}$$

For surface accumulation M is positive, and this profile can also be written as

$$T(z) - T_s = -\frac{G\sqrt{\pi}}{2kq}[\mathrm{erf}(zq) - \mathrm{erf}(Hq)]. \tag{6.24}$$

In this expression, erf(z) represents the error function, defined as

$$\mathrm{erf}(z) = \frac{2}{\sqrt{\pi}}\int_0^z \exp(-\bar{z}^2)\, d\bar{z}. \tag{6.25}$$

This function is tabulated in mathematical handbooks (for example, Abramowitz and Stegun, 1965) or available as standard routine in mathematical software packages.

In Figure 6.2 temperature profiles are shown for various values of the surface mass balance for a 3000 m thick ice sheet with a basal temperature gradient equal to

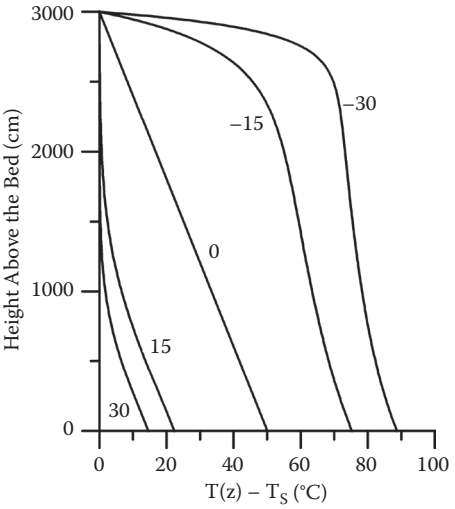

FIGURE 6.2 Steady-state temperature profiles according to the Robin temperature model. Labels indicate the surface accumulation rate in centimeters of ice depth per year. Profiles for positive surface accumulation were calculated using the analytical solution (6.24), while profiles for surface ablation were obtained by numerically integrating the thermodynamic equation (6.18) until a steady state was reached.

–0.0167 K/m. Profiles for negative values of M (that is, surface ablation) were calculated by numerically integrating the temperature equation (6.18) using (6.19) for the vertical velocity at depth, until a steady state was reached.

As shown by the curves in Figure 6.2 surface accumulation (or ablation) has a large effect on the steady-state temperature distribution. For M = 0, the temperature increases linearly with depth, with a gradient equal to the prescribed basal gradient. Surface accumulation results in considerable cooling of the glacier. For M = 0.3 m/yr, the upper half of the glacier is almost isothermal with a temperature equal to the surface temperature. Surface ablation, on the other hand, results in a much warmer glacier. This is a direct consequence of the parameterization of the vertical velocity used in this model; if M < 0, the ice flows upward, bringing warmer deep ice to the surface. Of course, these profiles are not very realistic; if surface ablation occurs, the surface temperature may be expected to be close to the melting temperature; and with temperatures increasing with depth, this would imply melting at all depths, which violates the first assumption on which the temperature solution (6.22) is based.

The temperature difference between the surface and the base is found by setting z = 0 in equation (6.24) and

$$T_b - T_s = \frac{G\sqrt{\pi}}{2kq}\,\mathrm{erf}\left(\frac{MH}{2K}\right)^{1/2}. \tag{6.26}$$

The contour diagram in Figure 6.3 shows how the value of the basal gradient and the glacier thickness affect this temperature difference. Increasing the basal heat flux

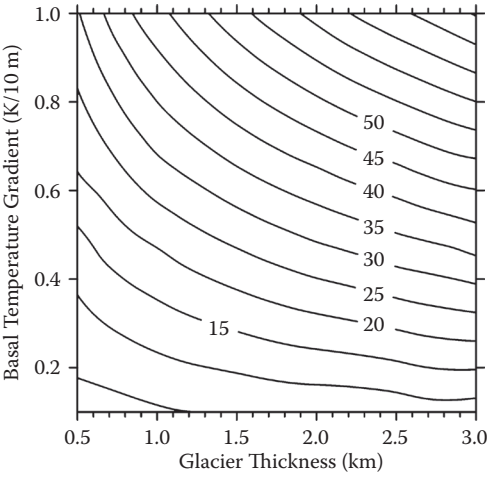

FIGURE 6.3 Temperature difference between the base and surface of a glacier as a function of the glacier thickness and temperature gradient at the base.

(or, equivalently, increasing the basal temperature gradient) increases the basal temperature, and thus the difference with the surface temperature. While the geothermal heat flux is poorly known, an average value is about $5 \cdot 10^{-2}$ W/m^2, corresponding to a basal temperature gradient of –0.02 K/m. Similarly, increasing the glacier thickness raises the basal temperature. Mathematically this follows immediately from the analytical solution. Physically, this can be understood by recalling that ice is a very good insulator; a thicker layer of ice traps more of the geothermal heat and allows less heat to escape through the upper surface.

The restriction that the basal temperature must be below the melting temperature can be relaxed, as was done by Weertman (1961b). Denoting the melting rate by M_b (positive if melting occurs), the vertical velocity at the base equals $-M_b$, and this term should be added to the right-hand side of equation (6.19) for the vertical velocity at depth. However, basal melt rates are typically of the order of mm/yr and this correction to (6.19) may be neglected. This means that the temperature profile derived above can still be applied if the basal temperature gradient is modified to include latent heat loss associated with melting. That is,

$$\left(\frac{\partial T}{\partial z}\right)_b = -\frac{G}{k} + \frac{L_f M_b}{k}. \tag{6.27}$$

This gradient can be estimated from the temperature difference between the upper surface and base of the glacier. Rearranging equation (6.26) and replacing G/k with the basal temperature gradient, gives

$$\left(\frac{\partial T}{\partial z}\right)_b = -\frac{2\, q (T_b - T_s)}{\sqrt{\pi}} \left[\operatorname{erf}\left(\frac{MH}{2K}\right)^{1/2} \right]^{-1}. \tag{6.28}$$

If melting or freezing occurs, the basal temperature is equal to the pressure melting temperature and the rate of basal melting can be estimated from equations (6.27) and (6.28).

The assumption that strain heating can be accounted for by increasing the geothermal heat flux is necessary to obtain an analytical solution for the temperature at depth. However, when solving the temperature equation numerically, as was done above for the case of surface ablation, this assumption is not necessary. Using the lamellar flow theory, discussed in Section 4.2, strain heating at depth can be calculated explicitly. To do so, the shear stress, τ_{xz}, is taken to increase linearly from zero at the surface to the maximum value, equal to the driving stress, at the base. The associated strain rate can be found by invoking the constitutive relation (2.10). Neglecting all other components of stress and strain rate, heat generated by internal deformation is then

$$W_d(z) = \frac{2A}{\rho C_p}\left(\frac{h - z}{H}\right)^4 \tau_{dx}^4, \tag{6.29}$$

where τ_{dx} represents the driving stress, h the elevation of the surface, and A the flow parameter. As discussed in Section 2.2, the flow parameter depends on the temperature of the ice. In the following calculation, the empirical relation (2.14) obtained by Hooke (1981) is used.

Strain heating affects only the temperature in the lower layers of an ice sheet. This is illustrated in Figure 6.4, which shows temperature profiles obtained by integrating

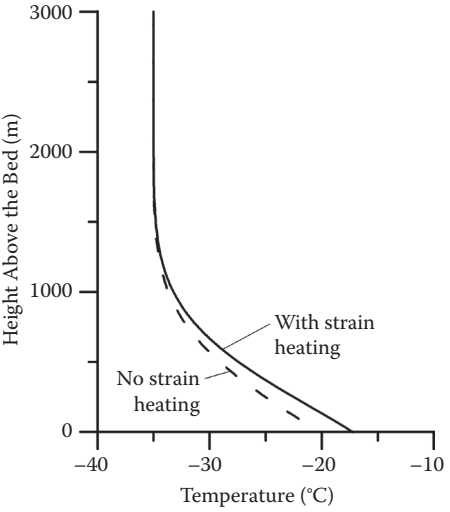

FIGURE 6.4 Steady-state temperature according to the Robin model. The solid line shows the profile calculated with inclusion of strain heating at depth (as estimated from the lamellar flow theory), and the dashed curve represents the profile without strain heating. Surface accumulation is 0.3 m/yr.

the temperature equation numerically until a steady state is reached. The full curve is the profile calculated with inclusion of strain heating at depth, while the dashed curve represents the profile without strain heating. All other parameters were kept the same for both calculations (τ_{dx} = 100 kPa, H = 3000 m, G = 0.042 W/m^2, T_s = –35°C). At the base, the temperature difference between both profiles is about 4°C. In this particular example, the effect of strain heating is small because the ice is relatively cold. The flow parameter, A, increases rapidly as the ice warms. This means that the warmer the ice, the more heat is generated by internal deformation, further raising the temperature, and so forth. It has been suggested that this positive feedback may lead to a runaway increase in temperature and deformation rate, called *creep instability.*

The most important shortcoming of the Robin temperature model is that horizontal advection of heat is neglected. How this affects the temperature distribution is discussed in the next section.

6.3 EFFECT OF HORIZONTAL HEAT ADVECTION

Observations in boreholes away from ice divides often show a reversed temperature gradient in the upper layers. The temperature decreases with depth to a minimum value, below which the ice becomes warmer with depth (c.f. the examples shown in Cuffey and Paterson, 2010, p. 415). In the Robin model, however, the upper layers are nearly isothermal or, where surface accumulation is sufficiently large, the temperature increases with depth from the surface down (Figure 6.2). This deficiency of the model is the direct consequence of neglecting horizontal advection of heat. To understand this, consider streamlines in an ice sheet, as schematically shown in Figure 6.5. These admittedly simplified streamlines represent the paths followed by ice originating at the surface. For the borehole AB, ice at depth C originated at a higher elevation than the surface ice at A. Because the surface temperature decreases with increasing elevation, this means that the ice at depth C is colder than the surface ice. In other words, the temperature decreases with depth until the effect of geothermal heat becomes important.

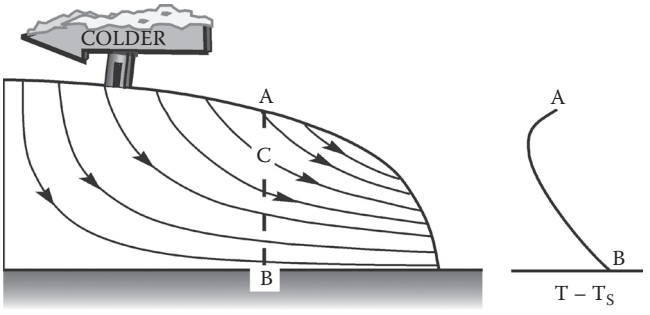

FIGURE 6.5 Simplified representation of streamlines in an ice sheet, illustrating the origin of the reversal of the temperature gradient at depth when horizontal advection becomes important. (Reproduced from Oerlemans, J., and C. J. van der Veen, *Ice Sheets and Climate,* Reidel Publ. Co., Dordrecht, 217 pp., 1984. With permission from Springer Verlag.)

Robin (1955) recognized this problem and derived an expression for the inverse temperature gradient near the surface by assuming that all terms in the heat-balance equation, with the exception of horizontal advection, are negligible. A more extensive treatment was given by Weertman (1968), in an effort to improve agreement between theoretical temperature profiles and that measured in the deep borehole at Camp Century in Greenland. The location of that borehole is far away from the ice divide, and horizontal advection of heat may be important.

Weertman (1968) estimated the horizontal temperature gradient at depth from the Robin profile given by equation (6.24). By choosing the x-axis in the mean direction of flow, only advection in the x-direction needs to be included in the temperature equation. Differentiating equation (6.24) with respect to x gives

$$\frac{\partial T}{\partial x} = \frac{\partial T_s}{\partial x} - \frac{\sqrt{\pi}}{2q^2}\gamma_b \frac{\partial q}{\partial x} \times$$
$$\times \left[\operatorname{erf}(zq) + \operatorname{erf}\left(\frac{z}{H}\right) + \left(\frac{2}{\pi}\right)^{1/2} zq \exp(-z^2 q^2) + \left(\frac{2}{\pi}\right)^{1/2} Hq \exp(-H^2 q^2) \right]. \tag{6.30}$$

In this expression, γ_b represents the vertical temperature gradient at the base of the glacier. After some arithmetic, equation (6.30) can be rewritten as

$$\frac{\partial T}{\partial x} = \frac{\partial T_s}{\partial x} + \frac{T(z) - T_s}{2}\left(\frac{1}{H}\frac{\partial H}{\partial x} - \frac{1}{M}\frac{\partial M}{\partial x}\right) +$$
$$- \frac{\gamma_b}{2q\sqrt{2}}\left(\frac{1}{H}\frac{\partial H}{\partial x} - \frac{1}{M}\frac{\partial M}{\partial x}\right)[zq \exp(-z^2 q^2) - Hq \exp(-H^2 q^2)]. \tag{6.31}$$

In his analysis, Weertman neglected the second line of this expression because it is negligibly small.

Also needed to estimate advection of heat is the horizontal velocity at depth. As in the preceding section, this velocity can be calculated from the lamellar flow theory. That is, the shear stress is taken to increase linearly with depth, which allows the shear strain rate to be calculated using the constitutive relation. Integrating this shear strain rate numerically, the horizontal component of velocity can be obtained (c.f. Section 4.2). Because the rate factor is temperature dependent, this procedure must be repeated for each time step when integrating the temperature equation to a steady state.

Inspection of equation (6.31) shows that the horizontal temperature gradient is controlled by three parameters, namely, the gradient in the surface temperature, the ice-thickness gradient, and horizontal gradients in surface accumulation. In most situations, the surface temperature and accumulation increase toward the margin of an ice sheet, while the thickness decreases away from the ice divide. This means that the horizontal temperature gradient at depth is generally smaller than that at the surface and may become negative near the base of the glacier.

TABLE 6.2
Camp Century Data

Ice thickness	H	1387.4 m
Thickness gradient	$\partial H/\partial x$	$-3.6 \cdot 10^{-3}$
Driving stress	τ_{dx}	45 kPa
Surface temperature	T_s	–24 °C
Surface temperature gradient	$\partial T_s/\partial x$	$2.2 \cdot 10^{-5}$ °C/m
Vertical temperature gradient at the base	γ_b	–0.0177 °C/m
Surface accumulation	M	0.36 m/yr
Gradient in surface accumulation	$\partial M/\partial x$	$2.5 \cdot 10^{-7}$ yr^{-1}

Source: Weertman, J., *J. Geoph. Res.,* 73, 2691–2700, 1968.

To investigate the importance of horizontal heat advection, the situation near the Camp Century borehole is considered. Data needed for the temperature calculation are taken from Weertman (1968) and given in Table 6.2. Using equation (2.14) to calculate the flow parameter, A, produces a horizontal velocity at the surface that is about a factor 3 less than that observed (3.3 m/yr). Therefore, A is multiplied by a constant factor to give the correct surface velocity. Figure 6.6 shows the results of five numerical integrations of the temperature equation, each differing by the processes included. Because the effects are so small, the difference between calculated temperatures and the Robin profile are shown in this figure. The Robin profile was obtained from equation (6.24) using the basal temperature gradient given in Table 6.2 and not including strain heating. To avoid introducing too many interactions at once, strain heating and the horizontal component of velocity were calculated only once for the calculations labeled 1–4, using the Robin temperature distribution to calculate the flow parameter.

Curve 1 in Figure 6.6 represents the calculation in which horizontal advection of heat is not included; differences between the calculated temperature profile and the Robin profile are entirely due to strain heating. Because the deformation rate and the shear stress are largest near the glacier base, deformational heating affects the lower part of the glacier only, raising the basal temperature by about 0.56°C. The effect of a horizontal gradient in surface temperature is illustrated by curve 2. Because the upglacial ice is colder, the temperature of the entire column decreases and a temperature inversion emerges. The inversion is rather small, however, somewhat more than 0.1°C, as compared with the 0.6°C inversion measured in the Camp Century borehole. The gradients in thickness and surface accumulation result in only minor changes in the temperature, as shown by the curves 3 and 4. Finally, including the interaction between temperature and ice flow by calculating the flow parameter each time step raises the temperature a few tenths of a degree (curve 5).

The modifications to the Robin theory proposed by Weertman (1968) have only a minor effect, and calculated corrections to the Robin temperature profile are less than about 0.5°C. As noted by Weertman (1968), this should not be very surprising because the horizontal velocity is small (3.3 m/yr at the surface) so that the third

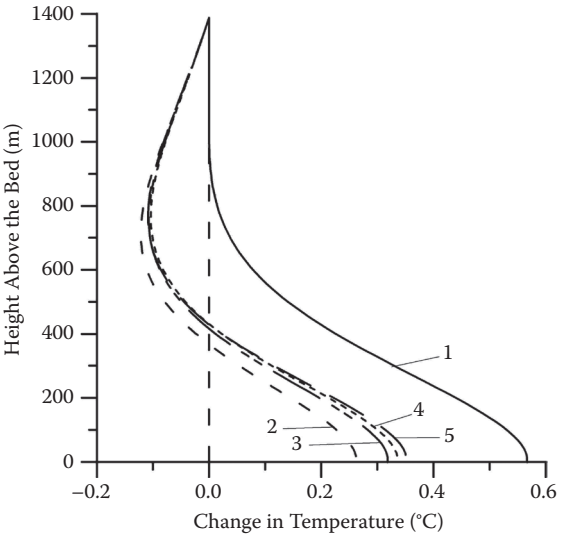

FIGURE 6.6 Effect of horizontal advection and strain heating on the Robin temperature profile (6.24), calculated using the data for Camp Century given in Table 6.2. For curves 1–4, strain heating and the horizontal component of velocity were calculated at the start of the integration only, using the Robin temperature profile to estimate the flow parameter at depth; for curve 5, strain heating and horizontal velocity were calculated each time step, using the result of the temperature calculation to estimate the flow parameter. Curve 1 shows the difference between the temperature calculated with inclusion of strain heating (no advection) and the Robin solution. Curve 2 represents the result of a calculation in which the horizontal temperature gradient at depth is taken equal to the temperature gradient at the surface. Curve 3 also includes the effect of the horizontal thickness gradient on the temperature gradient. Curves 4 and 5 represent calculations that include all terms of equation (6.31) but differ in how strain heating is included.

assumption of the Robin model (horizontal advection of heat may be neglected) is almost satisfied. The profiles in Figure 6.6 show that the effect of heat generated by internal deformation is as important as the effect of horizontal advection of heat.

The aim of Weertman's study was to improve agreement between the predicted and the measured temperature profile at Camp Century. Because the refinements of the temperature model did not substantially improve agreement, Weertman (1968) concluded that the borehole temperature reflects nonsteady conditions. That is, the ice temperature may currently be changing due to changing climatic conditions in the (recent) past. This point is taken up in more detail in the next section.

6.4 THERMAL RESPONSE OF A GLACIER TO CHANGES IN CLIMATE

The temperature distribution in ice sheets is determined by heat fluxes through the surface, the geothermal heat flux at the base, and heat generated by internal deformation. Considering the geothermal flux constant, changes in the ice temperature are

mostly initiated at the glacier surface, either by a change in surface temperature or by a change in surface accumulation or ablation. Changes in the thickness of the glacier or in the rate of deformation also affect the temperature distribution.

To study the effect of climate changes, consider as a start a simple harmonic variation in surface temperature:

$$T_s(t) = \Delta T \sin(\omega t), \tag{6.32}$$

where ΔT represents the amplitude of the surface perturbation and t denotes time. Neglecting for the time being downward advection (so vertical heat exchange is by diffusion only), the solution of the temperature equation (6.18) that satisfies this boundary condition, is

$$T(z,t) = \Delta T\, e^{-\overline{z}} \sin(\omega t - \overline{z}), \tag{6.33}$$

with

$$\overline{z} = (h-z)\left(\frac{\omega}{2K}\right)^{1/2}. \tag{6.34}$$

The amplitude of the perturbation decreases exponentially with depth, with the attenuation increasing with frequency. High-frequency variations penetrate only to shallow depths before being diffused away, while perturbations with a long time scale propagate much farther down into the glacier. Also, the time lag between the maximum perturbation at depth and at the surface increases with depth.

The depth at which the magnitude of the perturbation is 5% of the surface variation is

$$D(5\%) = \left(\frac{2K}{\omega}\right)^{1/2} \ln(20). \tag{6.35}$$

The phase shift between the perturbation at depth and that at the surface can be found by setting the time derivative of the temperature given by equation (6.33) to zero and is equal to $\ln(20)/\omega$. For example, the annual cycle has a period of 1 year ($\omega = 6.3\ \mathrm{yr}^{-1}$), and the 5% depth is 10 m. The maximum temperature perturbation at this depth occurs almost half a year after the temperature maximum at the surface. Because the annual cycle is almost completely diffused away before reaching a depth of 10 m, measured temperatures at this depth are often used as proxy for the annual mean surface temperature.

In the discussion so far, only vertical diffusion of heat was considered, allowing an analytical expression for the seasonal wave propagation to be derived. When advection is important, the temperature equation has to be integrated numerically to determine how the surface perturbation travels downward. Advection of heat greatly increases the depth to which the surface wave propagates. This is illustrated in Figure 6.7, which shows the downward penetration of a perturbation in surface temperature (with a period of 1000 yr), for the case of diffusion only (left panel) and

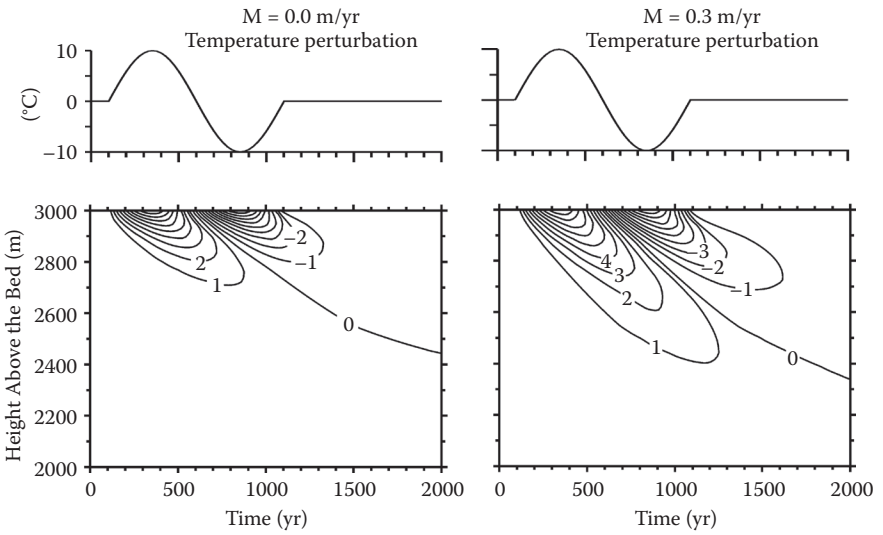

FIGURE 6.7 Downward penetration of a perturbation in the surface temperature by vertical conduction only (left panel) and including downward advection (right panel). Contours show the difference between the calculated temperature and the steady-state temperature at the start of the integration.

when downward advection is included. The downward motion advects the perturbation much deeper before it is diffused away. From this it may be concluded that surface accumulation is very important in determining the thermal response of a glacier.

As can be seen most clearly in the panel on the right of Figure 6.7, the cold wave does not penetrate as deeply as does the preceding warm wave. This is because part of the "excess" cold is used to remove the heat from the warm ice and bring its temperature to the initial Robin temperature. Only after the ice has reached this temperature does further cooling occur. If successive harmonic perturbations were to be prescribed, both the cold and the warm wave would penetrate to the same depth.

The vertical velocity is taken proportional to the rate of surface accumulation (equation (6.19)). Changes in accumulation affect the downward advection of cold surface ice to greater depth and modify the temperature distribution near the base of the glacier. This follows immediately from the steady-state profiles shown in Figure 6.2 and is further illustrated in Figure 6.8. Changes in the upper half of the glacier are negligibly small, while after an increase in surface accumulation, the increased downward transport of colder surface ice results in a lowering of the basal temperature. This calculation is not entirely realistic, however, because changes in accumulation affect the surface temperature also. If the air is colder than the snow surface, precipitation will tend to cool the surface. To account for this, the surface temperature needs to be calculated explicitly as a function of surface heat fluxes.

In the preceding calculations the surface temperature was prescribed as upper boundary condition, with the implicit understanding that this temperature equals

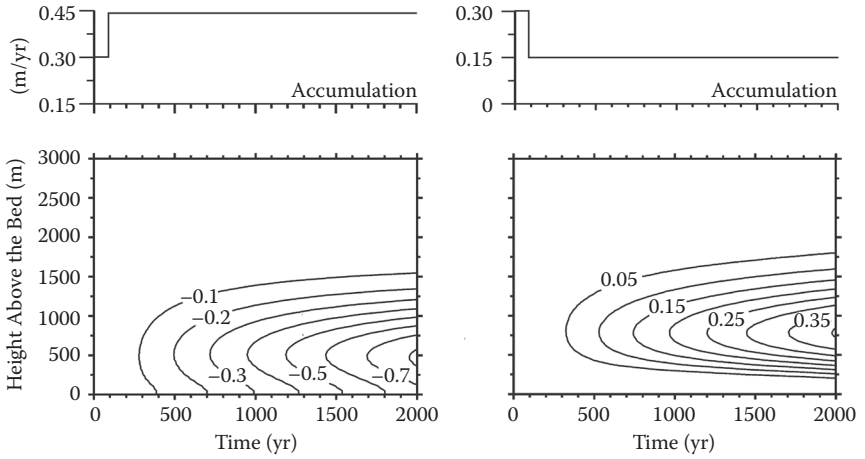

FIGURE 6.8 Effect of a stepwise increase (left panel) and decrease (right panel) on the temperature distribution in a glacier. Contours show the difference between the calculated temperature and the steady-state temperature at the start of the integration.

the air temperature. This is an appropriate approach when considering the temperature distribution in an ice sheet over long periods of time (for example, for modeling glacial cycles), mainly because the temperature at about 10 m below the surface is a good proxy for the annual air temperature if no surface melting occurs. For studying ice-sheet behavior on long time scales, detailed modeling of the thermal regime in the upper firn layers is not required (nor computationally feasible). However, for some applications, such detailed modeling is needed. For example, Van der Veen and Jezek (1993) calculate the temperature profile in the upper 65 m of the firn near Vostok Station in East Antarctica to study the seasonal changes in remotely sensed brightness temperatures. Another application is to investigate how climate conditions, and changes in these, affect surface ablation and englacial temperatures (for example, Greuell and Oerlemans, 1989a, b). In these studies, the surface energy balance replaces the air temperature as the upper boundary condition. The surface temperature of the firn is calculated from the requirement that the warming or cooling of the surface is directly proportional to the net flux of heat through the surface.

A schematic picture of the heat exchange between the atmosphere and the surface of a glacier is shown in Figure 6.9. Heat exchange is due to incoming and outgoing radiation (R_n), the latent heat flux ($L_f E$, with E the moisture flux), heat exchange associated with precipitation (Q_m), and the sensible heat flux (H). At the surface, the total energy flux is

$$Q_s = R_n + L_f E + H + Q_m. \tag{6.36}$$

Fluxes are taken positive when directed toward the glacier, that is, when providing heat to the glacier. It should be noted that Q_s does not represent the net flux through

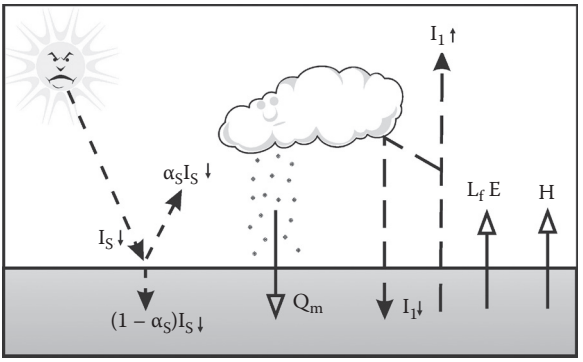

FIGURE 6.9 Schematic representation of the energy exchange between the atmosphere and glacier surface. Arrows with open heads indicate heat fluxes that can be directed either upward or downward, depending on the temperature difference between the glacier surface and the overlying air.

the surface layer, but only the net heat exchange between the atmosphere and glacier. The surface balance also depends on heat exchange with deeper layers of firn (c.f. Section 6.8).

The surface gains heat by incoming solar radiation, infrared long-wave radiation originating in the atmosphere, and loses heat by emitting long-wave radiation. The sensible heat flux acts as a heat source if the overlying air is warmer than the glacier surface, but represents a loss if the surface is warmer than the air above. Similarly, heat associated with precipitation can act as either a source or a sink, depending on the temperature of the precipitation reaching the surface. Where surface melting occurs, the downward percolation of meltwater serves to redistribute energy, warming deeper layers where refreezing occurs and latent heat is released. In addition, Phillips et al. (2010) propose that cryo-hydrologic warming could be a potential mechanism for rapid thermal response of glaciers to climate warming. Water present in englacial conduits (the cryo-hydrologic system) has a temperature that is at or above the pressure melting point. Thus, heat can be conducted from the conduits to the surrounding firn or ice. If some of the meltwater is retained after the melt season, substantial warming of the surrounding ice could occur. The magnitude of this warming depends on the spacing of meltwater conduits. Phillips et al. (2010) apply a numerical model to a location near the equilibrium line in West Greenland and find a substantial warming of ~10°C at 500 m below the surface 5 to 10 years after the onset of surface melting and cryo-hydrologic warming.

By coupling calculated surface fluxes to the thermodynamic equation (6.17), the change in firn temperature throughout the year or under altered climate conditions can be (numerically) calculated. An example of such a calculation is discussed in Section 6.8, but first, parameterizations that allow the surface fluxes to be calculated from observable meteorological variables are needed. In the next two sections, expressions for the radiative and turbulent surface heat fluxes are discussed. A more extensive treatment of this topic can be found in Greuell and Genthon (2003).

6.5 RADIATION BALANCE AT THE SURFACE OF A GLACIER

An extensive discussion of the radiation balance of the earth and atmosphere can be found in Peixoto and Oort (1992). Below, the most important results needed in energy-balance models of the glacier surface are discussed.

The earth receives its energy from the sun in the form of short-wave radiation with wavelengths ranging from ultraviolet, through the visible part of the spectrum, to the infrared. The average amount of solar radiation at the top of the atmosphere is called the *solar constant*, S (= 1395 W/m^2). To be exact, S is defined as the amount of solar radiation incident per unit area and per unit time on a surface normal to the direction of propagation and situated at the earth's mean distance from the sun (Peixoto and Oort, 1992). Of interest for the radiation balance is the amount of radiation through a horizontal surface. At the top of the atmosphere, this horizontal irradiance is

$$I_o = S \cos Z, \tag{6.37}$$

where Z represents the zenith angle of the sun. To be fully correct, this expression should include a factor that accounts for the varying distance between the earth and the sun. However, this correction factor is small (1.0344 in early January and 0.9646 in early July; Peixoto and Oort, 1992) and is usually neglected. The zenith angle, Z, is a function of geographical latitude, ϕ, solar declination, δ (the angular distance of the sun north [positive] or south [negative] of the equator), and hour angle, h (the angle through which the earth must rotate to bring the local meridian directly under the sun). Using spherical trigonometry, the following relation can be derived (for example, Sellers, 1965, p. 15)

$$\cos Z = \sin\phi \sin\delta + \cos\phi \cos\delta \cos h. \tag{6.38}$$

Tables of the solar declination are given in any standard ephemeris, while the hour angle follows directly from the local time in Greenwich Mean Time (GMT).

Not all solar radiation reaches the earth's surface. Part is absorbed in the atmosphere, while part is scattered by aerosols and clouds in the atmosphere. Scattering results in redirection of radiation, and part of the scattered radiation may reach the surface as so-called diffuse radiation. Goddard (1975) proposes the following expression for the average intensity of short-wave radiation reaching the surface:

$$I_s \downarrow = (1 - n\alpha_c)\, S\, T_r^{\sec Z} \cos Z, \tag{6.39}$$

where T_r represents an atmospheric turbidity coefficient (= 0.93 for Arctic pack ice simulations), n the cloud cover ($0 \le n \le 1$), and α_c the cloud albedo (ranging from 0.2 for cirrus clouds to around 0.7 for nimbostratus clouds; Houghton, 1985).

A more detailed parameterization for the short-wave solar radiation reaching the surface is used by Konzelmann et al. (1994), namely,

$$I_s \downarrow = f_{mr}\, \tau_{cs}\, \tau_{cl}\, S \cos Z. \tag{6.40}$$

Here τ_{cs} represents the clear-sky transmission and τ_{cl} the cloud transmission. The factor f_{mr} accounts for multiple clear-sky reflection. The clear-sky transmission is based on Beer's law for absorption of radiation in the atmosphere and is

$$\tau_{cs} = \gamma \exp(-\beta \tau_L m_r), \tag{6.41}$$

where m_r represents the relative optical air mass, τ_L the Linke turbidity factor, and $\gamma = 0.84$ and $\beta = 0.027$. The optical air mass is a measure of the distance that the solar radiation travels through the atmosphere, taking into account the lower density of the upper atmosphere, and is a function of zenith angle and elevation (or pressure). The Linke turbidity factor represents radiative transfer associated with scattering and absorption by air molecules, aerosols, ozone, and water vapor and is a function of the air temperature, vapor pressure, zenith angle, and elevation (as well as the ozone concentration, taken constant by Konzelmann et al., 1994). The multiple reflection term accounts for solar radiation reflected from the surface upward, and reflected downward again by clouds. Konzelmann et al. (1994) argue that high albedos introduce a significant increase in the global radiation compared with areas with low surface albedo, and therefore write the multiple-reflection coefficient as

$$f_{mr} = \frac{1}{1 - \alpha_a \alpha_s}, \tag{6.42}$$

where α_a and α_s represent the albedo of the air and the surface, respectively. Given that clouds reflect much more of the short-wave solar radiation, thus increasing the multiple reflection, than does a clear sky, it is not clear why this parameterization does not include the cloudiness, n. Finally, the cloud transmission coefficient, τ_{cl}, was determined by comparing daily mean global radiation measured at several sites on the Greenland Ice Sheet with calculated global radiation under clear-sky conditions. The measurements show that absorption of solar radiation by clouds is largest at low elevations and decreases with increasing elevation of the surface. In other words, the optical depth of clouds decreases with elevation. For the Greenland data, Konzelmann and others (1994) derive as best fit

$$\tau_{cl} = 1 - 0.78\, n^2\, e^{-0.00085h}, \tag{6.43}$$

with $0 \le n \le 1$, and h as the elevation of the surface in meters.

Perhaps the greatest uncertainty in estimating incoming solar radiation is associated with the role of clouds. As noted by Greuell and Genthon (2003), most parameterizations involve cloud cover only (n in equation (6.43)). However, what determines absorption of radiation by clouds is their optical thickness, which is more difficult to estimate. Fitzpatrick and others (2004) define a cloud transmittance, trc, as the ratio of incoming short-wave radiation at the surface when clouds are present to the amount of radiation that would reach the surface in the absence of clouds. They propose the following parameterization:

$$trc = \frac{a(\tau) + b(\tau)\cos Z}{1 + (c - d\alpha)\tau}, \tag{6.44}$$

where $a(\tau)$ and $b(\tau)$ are functions of the cloud optical depth, τ, Z is the solar zenith angle, and α is the surface albedo.

Part of the solar radiation reaching the glacier surface is reflected back to the atmosphere, as described by the albedo. For snow, the albedo is a function of grain size and density and may also be different for direct solar radiation and for diffuse solar radiation. Freshly fallen snow may reflect as much as 95% of the incoming radiation, while bare ice typically reflects about 50% to 60% of the radiation. For wet snow, the albedo is even smaller. Many different parameterizations for the albedo have been proposed, depending on the type of glacier studied. For example, in their study of ablation on alpine glaciers, Greuell and Oerlemans (1986) use an expression that links the albedo to the surface density, the rate of surface melting, cloudiness, and zenith angle. For polar ice caps, Greuell and Oerlemans (1989a) propose a much simpler formula, namely,

$$\alpha_s = \alpha_o + 0.06\,n, \tag{6.45}$$

where $\alpha_o = 0.8$ in the absence of meltwater at the surface and $\alpha_o = 0.54$ if meltwater is present. Greuell and Konzelmann (1994) model the albedo on the Greenland Ice Sheet as a function of the snow density at the surface, ρ_s, and cloud amount, n:

$$\alpha_s = \alpha_i + \frac{\rho_s - \rho_i}{\rho_{fs} - \rho_i}(\alpha_{fs} - \alpha_i) + 0.05(n - 0.5), \tag{6.46}$$

where the subscript fs refers to fresh snow ($\rho_{fs} = 300$ kg/m^3, $\alpha_{fs} = 0.85$) and the subscript i to glacier ice ($\rho_i = 910$ kg/m^3, $\alpha_i = 0.58$). In central East Antarctica, on the other hand, the albedo varies little (Schwerdtfeger, 1970), and a constant value may be used.

To be fully correct, albedo parameterizations should account for the age of the surface snow; as the snow settles after deposition, its structure and reflective properties change. In addition, the onset of melting has a large effect on the albedo. For example, on Haig Glacier in Alberta, Canada, Shea et al. (2005) measured a decrease in albedo from around 0.9 in mid-May to around 0.2 in mid-August. As melting ceased toward the end of the summer, the albedo increased rapidly to around 0.6 in early October and continued to rise throughout the winter. Further, the albedo depends on incidence angle and wavelength of the incoming radiation. For these reasons, then, it is no surprise that many different parameterizations have been proposed. For more extensive discussions, see Brock and others (2000) and Greuell and Genthon (2003). Table 6.3 gives typical albedo values for different types of snow and ice surfaces.

Part of the short-wave radiation penetrates into the upper firn layers. The amount of absorption depends on the wavelength of the radiation as well as on the physical properties of the firn. Holmgren (1971, Part E) describes experiments conducted in the upper 18 cm of firn on Devon Island Ice Cap. These data show that minimum extinction occurs for wavelengths near the middle part of the visible spectrum, while for longer wavelengths, the extinction coefficient increases markedly.

TABLE 6.3
Typical Values for the Albedo of Snow and Ice, Based on a Literature Review by S.J. Marshall

Surface Type	Recommended	Range
Fresh dry snow	0.85	0.75–0.98
Old clean dry snow	0.80	0.70–0.85
Old clean wet snow	0.60	0.46–0.70
Old debris-rich dry snow	0.50	0.30–0.60
Old debris-rich wet snow	0.40	0.30–0.50
Clean firn	0.55	0.50–0.65
Debris-rich firn	0.30	0.15–0.40
Superimposed ice	0.65	0.63–0.66
Blue ice	0.64	0.60–0.65
Clean ice	0.35	0.30–0.46
Debris-rich ice	0.20	0.06–0.30

Source: Reprinted from Cuffey, K. M., and W. S. B. Paterson, *The Physics of Glaciers* (4th ed.), Butterworth-Heinemann, Burlington, MA, 693 pp., 2010. With permission from Elsevier.

For coarse-grained snow, the attenuation of solar radiation is about twice as deep as for fine-grained snow. Greuell and Oerlemans (1989a) make the assumption that all radiation with wavelengths greater than 0.8 μm (about 36% of the solar radiation penetrating the surface) is completely absorbed in the surface layer. The remaining 64% is extinguished at depth according to Beer's law. Thus, solar radiation absorbed by the glacier surface is

$$I_s(h) = 0.36\,(1 - \alpha_s)\,I_s\downarrow, \tag{6.47}$$

while the radiative flux at depth is

$$I_s(h - z) = 0.64\,(1 - \alpha_s)\,e^{-\beta(h-z)}\,I_s\downarrow. \tag{6.48}$$

The extinction coefficient, β (in m^{-1}), decreases linearly with increasing firn density as

$$\beta = -0.012\,\rho_s + 14.706. \tag{6.49}$$

In a later study, Greuell and Konzelmann (1994) obtained values for β that are about twice as large, by optimizing the fit between calculated and measured temperature profiles.

Kuipers Munnike et al. (2009) compare results from an energy-balance model with measurements of the surface energy balance, including subsurface firn temperature, at Summit, Greenland. They find that, on average, 6.3% of the incoming solar radiation is absorbed at depths greater than 0.5 cm below the surface. Penetration of

short-wave radiation into the firn has an important effect on modeled firn temperatures. Not including this term in the energy-balance model results in a decrease in firn temperature of ~4°C in the upper 1 m.

The second source of energy for the glacier surface is long-wave radiation emitted by water vapor and other greenhouse gases in the atmosphere. Of these gases, water vapor accounts for about 80% of the total long-wave radiation (Male, 1980). Hence, variations in incoming long-wave radiation are mainly due to changes in the water content of the atmosphere and in its temperature. In most studies, the atmospheric radiation is related to humidity and temperature at "screen level," usually anywhere from 1 to 10 m above the surface. This appears to be a reasonable approximation because most of the long-wave radiation reaching the surface originates from the lower part of the atmosphere (Geiger, 1966).

For clear-sky conditions, the incoming long-wave radiation is most often estimated using the expression due to Brunt (1939)

$$I_l \downarrow = \sigma T_a^4 (a + b\sqrt{e_a}), \tag{6.50}$$

where $\sigma = 5.6704 \cdot 10^{-8}\ \mathrm{W/m^2K^4}$ represents the Stefan–Boltzmann constant, T_a the air temperature at about 2 m above the surface, and e_a the water vapor pressure at that level. Greuell and Oerlemans (1986) use a somewhat different parameterization,

$$I_l \downarrow = \varepsilon_a \sigma T_a^4, \tag{6.51}$$

with the clear-sky emissivity related to water vapor pressure (in Pa) and air temperature (in K) as

$$\varepsilon_a = 0.70 + 5.95 \cdot 10^{-7} e_a e^{1500/T_a}. \tag{6.52}$$

Greuell and Oerlemans (1986) argue that the contribution from clouds to the downward long-wave radiation may be treated as a separate radiation flux, parameterized as

$$I_{lc} \downarrow = \varepsilon_c n f_w \tau_w \sigma T_{cl}^4. \tag{6.53}$$

In this expression, T_{cl} represents the temperature of the clouds, ε_c the emissivity of clouds (about 1.0 for dense clouds, and 0.5 for cirrus clouds), f_w the fraction of blackbody radiation emitted in the atmospheric window (8–14 μm) that can be transmitted to the surface, and τ_w the transmittance of the atmosphere for this atmospheric window. The net incoming long-wave radiation according to Greuell and Oerlemans (1986) is given by the sum of equations (6.51) and (6.53).

Goddard (1975) uses a simpler expression to estimate incoming long-wave radiation. The effect of clouds is included by introducing an effective sky emissivity, ε_2, which equals 1 for completely overcast skies, and 1.14 under cloud-free conditions, and

$$I_l \downarrow = \varepsilon_2 C \sigma T_a^6. \tag{6.54}$$

The parameter C is an empirical constant (= $9.35 \cdot 10^{-6}$). This expression does not take into account the effect of water vapor on the atmospheric radiation. A comparable formula is used by Konzelmann et al. (1994). The effective emittance is the weighted mean of the clear-sky emittance, ε_{cs}, and the emittance of a completely overcast sky, ε_{oc}, so that, for completely overcast skies, the parameterization does not include the clear-sky emittance:

$$I_l \downarrow = \left[\varepsilon_{cs}(1 - n^p) + \varepsilon_{oc}\, n^p\right]\sigma T_a^4. \tag{6.55}$$

The clear-sky emittance is calculated from a somewhat modified form of the expression derived analytically by Brutsaert (1975):

$$\varepsilon_{cs} = 0.23 + b\left(\frac{e_a}{T_a}\right)^{1/m}. \tag{6.56}$$

Using various data collected in Western Greenland, Konzelmann et al. (1994) find an optimal fit between model prediction and measurements for b = 0.443 and m = 8 in equation (6.56), $\varepsilon_{oc} = 0.952$ and p = 4 in (6.55) if instantaneous cloud observations and hourly radiation measurements are used, and $\varepsilon_{oc} = 0.963$ and p = 3 if daily mean observations are used.

The third and final radiative flux that needs to be considered is long-wave radiation emitted by the glacier surface. This radiation, with wavelengths in the range of 5–40 μm, is confined to the snow surface and can be estimated from the Stefan–Boltzmann radiation law

$$I_l \uparrow = \varepsilon_o\, \sigma\, T_s^4. \tag{6.57}$$

The emissivity of snow, ε_o, varies typically between 0.98 and 1.0. Goddard (1975) includes the effect of clouds on the outgoing radiation (part of which is reflected back to the surface) by introducing a long-wave cloud-reduction coefficient, k_c:

$$I_l \uparrow = (1 - n\, k_c)\varepsilon_o\, \sigma\, T_s^4. \tag{6.58}$$

In simulations for Arctic pack ice, Goddard (1975) uses $k_c = 0.75$ under clear-sky conditions and $k_c = 0.73$ for cloudy conditions.

In general, the degree of sophistication used in modeling the radiative fluxes depends on the extent of meteorological observations. If few such observations are available, there is not much point in using very sophisticated models that cannot be tested or calibrated, and a parameterization such as equation (6.39) should be adequate. On the other hand, where extensive measurements have been conducted, including measurements of radiation, more complicated radiation models may be warranted. Of course, one could argue that if actual radiation measurements are available, one might as well use these observations when considering the energy exchange between the atmosphere and glacier surface. However, the implicit assumption behind the

more complex models is that these models can also be applied to time periods when fewer meteorological observations are available, as well as to different locations.

The expressions discussed above apply only to situations where the glacier surface is not shielded by surrounding mountains. For small alpine glaciers, the surrounding valley walls may block part of the solar radiation as well as cause significant changes in the long-wave radiative fluxes. By obscuring part of the sky, valley walls reduce the incoming atmospheric radiation. General expressions to describe these effects cannot be given because they are determined by the particular geometry of the glacier and its surroundings.

6.6 TURBULENT HEAT FLUXES

The sensible heat flux is due to the difference in temperature of the surface of the glacier and the air above. The heat exchange is accomplished mainly by turbulent motion in the boundary layer, except perhaps in the first few millimeters above the surface, where molecular diffusion may be more important. For the latent heat flux, the transfer of heat is indirect and associated with evaporation at the surface and subsequent condensation at higher levels in the atmosphere (or vice versa). If the rate of evaporation equals E, the amount of heat needed for evaporation is, per unit time, $L_f E$, where L_f represents the latent heat of evaporation or condensation (that is, the amount of heat needed to evaporate 1 kg of water or condensate the corresponding amount of water vapor). This heat is extracted from the immediate surroundings (for example, the glacier surface) and released where condensation takes place. The ratio of the sensible heat flux to the latent heat flux is called the Bowen ratio.

The motion in the boundary layer is strongly influenced by the friction generated at the surface, and the wind profile exhibits large vertical shear because the speed must be zero at the surface. As a result, and because of the heating or cooling of the surface, turbulent flow develops, in which random velocity perturbations are superimposed on the average flow. This turbulent mixing of air is a very effective process by which properties such as momentum, heat, water vapor, or aerosols are redistributed vertically. To estimate the flux of any quantity (or net vertical transport) at the surface, the assumption is usually made that the flux in the lower few meters of the boundary layer is representative of the flux at the surface. This allows the fluxes to be estimated from standard meteorological observations, such as wind speed, air temperature, and humidity.

To arrive at an expression for the turbulent flux of a quantity F, the continuity equation for that quantity needs to be considered. While molecular diffusion may be important in the thin sublayer very close to the surface, vertical transport is mainly determined by vertical motion in the boundary layer, and if there is no local production or loss, F changes with time as a result of advection only. Denoting the three orthogonal directions by the subscript i, and using the summation convention for repeat indexes, the continuity equation is

$$\frac{\partial F}{\partial t} = - U_i \frac{\partial F}{\partial x_i}, \tag{6.59}$$

where U_i represents the three components of velocity in the boundary layer.

Turbulent flow is characterized by random velocity variations superimposed on the average velocity. Thus, the total velocity in the x_i-direction, U_i, may be written as

$$U_i = \bar{U}_i + \tilde{u}_i, \tag{6.60}$$

where the overbar denotes the average flow, defined as

$$\bar{U}_i = \lim_{T\to\infty} \frac{1}{T} \int_{t_o}^{t_o+T} U_i \, dt. \tag{6.61}$$

The tilde denotes the random fluctuation in velocity. By definition, the time average of this term is zero. In the meteorological literature, this partitioning is referred to as Reynolds decomposition (for example, Tennekes and Lumley, 1972).

A decomposition similar to (6.60) for the velocity can be introduced for the quantity under consideration, F, and substitution in the continuity equation (6.59) yields

$$\frac{\partial}{\partial t}(\bar{F} + \tilde{f}) = -(\bar{U}_i + \tilde{u}_i) \frac{\partial}{\partial x_i}(\bar{F} + \tilde{f}). \tag{6.62}$$

The average flow is assumed to be in steady state, so that taking the time average of this expression gives

$$0 = -\bar{U}_i \frac{\partial \bar{F}}{\partial x_i} - \overline{\tilde{u}_i \frac{\partial \tilde{f}}{\partial x_i}}. \tag{6.63}$$

In the boundary layer, the air may be considered incompressible, that is, having a constant density. By substituting the decomposition of velocity in an average and a fluctuation term into the incompressibility condition and taking the time average, it follows that both the mean flow and the turbulent velocity fluctuations are incompressible (c.f. Tennekes and Lumley, 1972, p. 30). Thus,

$$\frac{\partial \tilde{u}_1}{\partial x_1} + \frac{\partial \tilde{u}_2}{\partial x_2} + \frac{\partial \tilde{u}_3}{\partial x_3} = 0. \tag{6.64}$$

Equation (6.63) can now be rewritten as

$$\bar{U}_i \frac{\partial \bar{F}}{\partial x_i} = -\frac{\partial}{\partial x_i}\left(\overline{\tilde{u}_i \tilde{f}}\right). \tag{6.65}$$

The right-hand side may be considered as the divergence of a flux, with the mean turbulent flux of the quantity F per unit area and unit time given by

$$Q_i = \overline{\tilde{u}_i \tilde{f}}. \tag{6.66}$$

Of interest to the energy budget are the vertical fluxes of sensible and latent heat. The sensible heat flux, H, follows by taking $F = \rho_a C_{pa} T$ and considering the vertical direction only

$$H = \rho_a C_{pa} \overline{\tilde{w}\tilde{t}}. \tag{6.67}$$

In this expression, $\tilde{w}$ represents the fluctuation in the vertical velocity (that is, $\tilde{w} = \tilde{u}_3$ in the notation used above), and $\tilde{t}$ the temperature perturbation. Similarly, the vertical flux of moisture is

$$E = \rho_a \overline{\tilde{w}\tilde{q}}, \tag{6.68}$$

where q represents the specific humidity (in kg of water vapor per kg of air).

The next step is to relate the perturbations to the average field. This is commonly done using the mixing-length theory developed by Prandtl (1932) (c.f. Schlichting, 1968; Peixoto and Oort, 1992). In Prandtl's model, a parcel of air originally at level z moves over a vertical distance ℓ, keeping its original velocity, before being absorbed and assuming the velocity of its surroundings. The difference between the speed of the parcel and its surroundings is a measure for the turbulent fluctuations so that

$$\begin{aligned} \tilde{u} &= \bar{U}(z) - \bar{U}(z+\ell) = \\ &= -\ell \frac{\partial \bar{U}}{\partial z}. \end{aligned} \tag{6.69}$$

It seems reasonable to make the assumption that the mixing length, ℓ, is proportional to the physical space available; that is, ℓ is taken proportional to the distance to the surface as $\ell = kz$, where $\kappa = 0.4$ is the Von Kármán constant. A friction velocity, U_*, is now introduced such that

$$\begin{aligned} \left| \frac{\partial \bar{U}}{\partial z} \right| &= \frac{U_*}{\ell} = \\ &= \frac{U_*}{\kappa z}. \end{aligned} \tag{6.70}$$

Integrating this expression with respect to z gives the often-used logarithmic wind profile

$$\bar{U}(z) = \frac{U_*}{\kappa} \ln \frac{z}{Z_o}. \tag{6.71}$$

Here, Z_o represents the roughness length of the surface, that is, the height above the surface at which the average wind speed is zero. Greuell and Konzelmann (1994) use $Z_o = 0.12$ mm for snow before melting, $Z_o = 1.3$ mm for snow after melting, and $Z_o = 3.2$ mm for ice, based on observations of wind speed over the Greenland Ice Sheet. The friction velocity, U_*, is typically of the order of 0.2 to 0.4 m/s.

If the turbulence is isotropic, the magnitude of velocity perturbations is the same in all directions. In particular

$$|\tilde{w}| = \ell \left| \frac{\partial \bar{U}}{\partial z} \right|. \tag{6.72}$$

For other variables, such as temperature, a similar relation between fluctuation and average vertical gradient is assumed. That is

$$|\tilde{t}| = \ell \left| \frac{\partial \bar{T}}{\partial z} \right|. \tag{6.73}$$

Equation (6.67) for the sensible heat flux can now be written as

$$H = \rho_a C_{pa} \kappa z U_* \frac{\partial \bar{T}}{\partial z}. \tag{6.74}$$

In the following, the overbar is omitted, with the understanding that meteorological quantities refer to time averages (obtained from observations). An expression similar to (6.74) can be given for the vertical flux of moisture.

The final step is to relate the friction velocity and vertical temperature gradient to observations. If U_{ref} represents the measured wind speed at some level Z_{ref}, it follows from the logarithmic wind profile (6.71) that the friction velocity is

$$U_* = \frac{\kappa Z_{ref}}{\ln(Z_{ref}/Z_o)}. \tag{6.75}$$

Analogous to the derivation of the logarithmic wind profile, a logarithmic profile can be derived for the temperature in the boundary layer, with a temperature scale, T_*, given by an expression similar to equation (6.75). For simplicity, often assumptions are made that the roughness length for temperature and wind speed are the same and that both quantities are measured at the same level. This is not necessary but simplifies the expressions for the turbulent heat fluxes.

Using the expressions derived above, the turbulent heat fluxes can now be expressed in terms of measurable meteorological variables. The sensible heat flux becomes

$$H = \rho_a C_{pa} \kappa^2 U_{ref} (T_{ref} - T_s)[\ln(Z_{ref}/Z_o)]^{-2}. \tag{6.76}$$

Note that the surface temperature, T_s, appears in this expression because T_s is not zero (contrary to the wind speed, assumed to be zero at the surface). The corresponding expression for the latent heat flux is

$$L_f E = L_f \rho_a \kappa^2 U_{ref} (q_{ref} - q_s)[\ln(Z_{ref}/Z_o)]^{-2}. \tag{6.77}$$

It may be noted that some authors use the potential temperature, rather than the physical temperature, to calculate the flux of sensible heat. The potential temperature is

defined as the temperature that a parcel of air would attain if the pressure is changed adiabatically from the actual pressure, P, to the reference pressure, P_o (usually taken equal to 1000 mbar). Near the surface, the actual pressure is close to the reference pressure and both temperatures are almost the same and within measurement uncertainty.

The approximation (6.70) implies that the vertical flux of momentum is constant with height (Peixoto and Oort, 1992). This is true where the surface is smooth and the boundary layer is in neutral equilibrium. That is, when the vertical temperature gradient equals minus the dry-adiabatic lapse rate, $\gamma_d = g/C_{pa} \approx 9.8\,K/km$. Where the actual temperature gradient is less than $-\gamma_d$, the thermal stratification is unstable, while the stratification is stable where $\partial T/\partial z > -\gamma_d$. In a nonneutral atmosphere, the turbulence acts against the buoyancy forces, which results in an additional upward heat flux in an unstable atmosphere and a downward flux of heat in a stable boundary layer (Busch, 1973). While analytical expressions for the deviations from logarithmic have not been obtained, the Monin–Obukhov similarity theory has been used to establish semi-empirical profiles (for example, Businger, 1973). Because no theoretical solution for the profiles exists, there is still considerable debate as to the form of the correction to the logarithmic profile. Grainger and Lister (1966) conclude that the logarithmic profile applies best to a neutral and extremely stable atmosphere, while a power law may be more appropriate for a moderately stable boundary layer. Holmgren (1971, Part B) argues that observations on Devon Island Ice Cap do not support the Monin–Obukhov theory under stable conditions. Goddard (1975) parameterizes the sensible and latent heat fluxes by adopting a log plus linear profile plus a universal function dependent on the Richardson number. Stearns and Weidner (1993) use an iterative procedure to determine the heat fluxes from measured wind speed and temperature difference. In particular where katabatic winds develop, with a maximum in wind speed a few meters above the surface, important differences between predictions based on the Monin–Obukhov theory and observations have been noted (Denby, 1999; Greuell and Genthon, 2003).

A major uncertainty in determining turbulent fluxes is the roughness length of the surface, Z_o (Munro, 1989; Braithwaite, 1995). An order of magnitude increase in the value of Z_o results in a doubling of the calculated turbulent heat fluxes (Brock et al., 2000). By definition, the roughness length is the height above the surface at which the average wind vanishes and, in principle, can be determined by extrapolating the wind speed profile (Munro, 1989). The difficulty with this extrapolation is that the surface of glaciers and ice sheets is irregular with small-scale features such as wind-blown sastrugi disturbing the flow of air up to a height of about twice the height of the main surface roughness elements (Smeets et al., 1999). Above this roughness-induced sublayer, wind profiles behave as expected for an idealized homogeneous surface. Alternatively, Z_o can be estimated from the small-scale roughness of the snow surface (Van der Veen et al., 1998, 2009) although it is not immediately evident which spatial scale of roughness elements determines Z_o (Munro, 1989). A review of estimated roughness values is given by Brock and others (2006) and shows a range from 0.004 mm for snow on the Antarctic Plateau, to up to 80 mm for very rough glacier ice. Typical ranges are summarized in Table 6.4.

TABLE 6.4
Typical Range of Values for the Roughness Length for Various Snow and Ice Surfaces

Surface Type	Range (mm)
Smooth ice	0.01–0.1
New snow and polar snow	0.05–1
Snow on low-latitude glaciers	1–5
Ice in ablation zone	1–5
Coarse snow with sastrugi	11
Rough glacier ice	20–80

Source: Based on Brock, B. W., I. C. Willis, and M. J. Sharp, *J. Glaciol.*, 52, 281–297, 2006.

The flux parameterizations (6.76) and (6.77) contain the same roughness length, Z_o. However, close to the surface the vertical exchange of momentum is by molecular diffusion and by pressure forces against obstacles, while transfer of heat and water vapor results from pressure forces only. This difference leads to two different roughness scales. Andreas (1987) derived expressions relating both roughness scales to Z_o. Observations appear to be somewhat ambiguous regarding the applicability of these parameterizations (c.f. Greuell and Genthon, 2003).

6.7 PHYSICAL PROPERTIES OF FIRN

The values of thermal parameters given in Table 6.1 apply to solid glacier ice and may be used in most ice-sheet models. However, for freshly fallen snow and in the upper firn layers of a glacier, the thermal properties are significantly different from those of solid ice. For example, the density at the glacier surface is about 350 kg/m^3, compared with 917 kg/m^3 for solid ice. These differences are important when considering the evolution of near-surface temperatures and therefore should be included in the calculation of these temperatures. A complete review of the subject and all relevant data can be found in Yen (1981). Below, only the most important relations are summarized.

The heat capacity, C_{pa}, is defined as the amount of heat needed to increase the temperature of a unit mass by 1 degree, keeping the pressure constant. Data from different experimental studies are consistent and show a linear relation between the heat capacity and temperature, T. For the temperature range most relevant to glacier studies (T > 150 K), Yen (1981) finds as best fit

$$C_{pa} = 152.456 + 7.122\,T, \tag{6.78}$$

with the heat capacity in $\mathrm{J\,kg^{-1}K^{-1}}$ and the temperature in K. For temperatures below 150 K, the heat capacity may also be expressed as a linear function of temperature but with different coefficients (given in Yen, 1981).

The thermal conductivity, k, introduced as the constant of proportionality in Fourier's law for heat conduction (equation (6.11)) depends on density and temperature. For solid ice, a regression analysis of all available data suggests (Yen, 1981)

$$k_i = 9.828 \cdot e^{-0.0057T}, \tag{6.79}$$

with k_i in $\mathrm{W\,m^{-1}K^{-1}}$ and T in K. For snow, the transfer of heat is a more complex process, involving conduction and convection, as well as diffusion of water vapor. Measurements of conductivity often include all these processes, and therefore k is often replaced by the effective thermal conductivity, k_e. In most experimental studies, the effective conductivity is correlated with snow density. Yen (1981) shows that all data can be reasonably represented by

$$k_e = 2.22362 \left(\frac{\rho_f}{1000} \right)^{1.885}, \tag{6.80}$$

where k_e is expressed in $\mathrm{Wm^{-1}K^{-1}}$, and the density of firn, ρ_f, in $\mathrm{kg/m^3}$. Pitman and Zuckerman (1967) investigated how temperature affects the effective conductivity, using vapor-grown ice crystals and conducting measurements at various temperatures and densities. Except for the lowest densities (about 100 $\mathrm{kg/m^3}$), their data suggest the following relation (Yen, 1981):

$$k_e = 0.0688 \exp(0.0688 T_c + 4.6682 \cdot 10^{-3} \rho_f), \tag{6.81}$$

where T_c represents the firn temperature in °C. The actual thermal conductivity is often described by Van Dusen's equation (Van Dusen, 1929):

$$k = 2.1 \cdot 10^{-2} + 4.2 \cdot 10^{-4} \rho_f + 2.2 \cdot 10^{-9} \rho_f^3. \tag{6.82}$$

Paterson suggests that this formula gives a lower limit for the conductivity; an upper limit can be found by the expression derived by Schwerdtfeger (1963) based on Maxwell's work on the electrical conductivity of heterogeneous media:

$$k = \frac{2 k_i \rho_f}{3\rho_i - \rho_f}. \tag{6.83}$$

Here, k_i and ρ_i represent the conductivity and density of ice, respectively.

As a result of many processes, the firn density increases with depth. Density changes in snow are caused by (Yen, 1981): (1) compaction due to the weight of snow above, (2) destructive metamorphism (that is, sharp-edged freshly fallen snow crystals are smoothed by migration of water molecules, resulting in settling and increase in density), (3) constructive metamorphism (transfer of vapor within the snow cover due to the temperature gradient), and (4) melt metamorphism (the change in snow structure due to melt-freeze cycles and the change in crystals as a result of the presence of meltwater). Yen (1981) summarizes various models proposed to parameterize each of these processes.

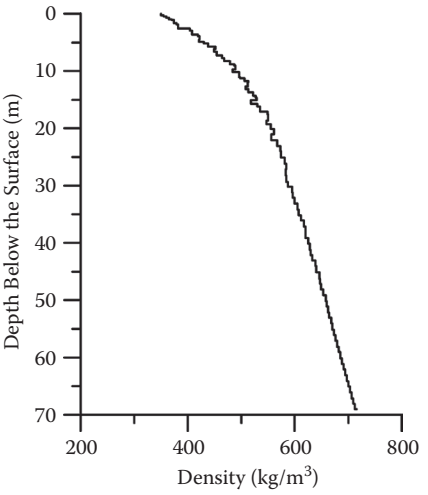

FIGURE 6.10 Density as a function of depth as measured at South Pole, Antarctica. (Based on data from Hogan, A. W., and A. J. Gow, *Geoph. Res.,* 102(D), 14021–14027, 1997.)

At present, most studies use empirical or semiempirical expressions. Figure 6.10 shows the depth–density profile measured at South Pole, Antarctica (Hogan and Gow, 1997). In good approximation, the profile to a depth of 65 m below the surface may be represented by

$$\rho_f(d) = 380.92 + 11.46d - 0.16d^2 + 8.85 \cdot 10^{-4} d^3, \tag{6.84}$$

where d denotes the depth below the surface in m. Another empirical relation adopts an exponential increase with depth according to

$$\rho_f(d) = \rho - (\rho - \rho_s) e^{-Cd}, \tag{6.85}$$

where $\rho = 917$ kg/m^3 is the density of solid ice, ρ_s the density of surface snow, and C a site-specific constant (Schytt, 1958).

The implicit assumption behind density profiles (6.84) and (6.85) is that the firn density does not change with time at any location and depth. This is known as Sorge's law, which states that when snow accumulates steadily and there is no melting, at any particular location the density is always the same at any one depth below the surface. This law was suggested by Bader (1954) based on observations made by Ernst Sorge in Greenland during the winter of 1930–1931 in a 16 m deep hand-dug pit. For many modeling applications, temporal variations in firn density may be ignored and simple steady-state firn densification models are adequate. A notable exception is when considering interannual variability in snowfall and associated short-term elevation changes (Arthern and Wingham, 1998; Helsen et al., 2008).

Where surface melting occurs, the downward percolation of meltwater, as well as internal melting due to the absorption of penetrating short-wave radiation, dominates

the densification process. Water movement through snow is a complex process that depends on the presence of vertical drainage channels, ice layers, the slope of the surface, and many other factors. A review of theories for water flow is presented by Male (1980), but none of these is readily implemented into a numerical model. In their numerical model, Greuell and Konzelmann (1994) apply a three-step procedure to simulate the downward percolation of meltwater. First, if the calculated temperature at any grid element exceeds the melting temperature, the temperature is set equal to the melting temperature and the excess heat used for melting and the amount of meltwater formed added to the water content of the grid element. Next, downward percolation and refreezing are simulated, starting at the surface (the uppermost grid element). Refreezing is limited by the condition that the temperature of the firn cannot exceed the melting temperature (refreezing releases latent heat, thus raising the firn temperature), and by the available meltwater and pore space. Some of the meltwater that remains after calculating the amount of refreezing may actually remain in the grid element (instead of percolating downward) as capillary water (that is, water retained against gravity in the pores of the firn). There is a maximum of water that can be retained this way, given by the maximum of the ratio of capillary water to pore volume, the so-called irreducible water amount. If the amount of meltwater present exceeds the irreducible water amount, the water content of the grid element is set equal to this maximum and the remainder is added to the next deeper grid element. This procedure may result in the collection of meltwater in the lowermost grid element. In reality, meltwater is likely to percolate downward until encountering an impermeable ice layer. Some of the meltwater may run off on top of this layer, while some of the meltwater may form a slush layer of snow saturated with water. Greuell and Konzelmann (1994) do not explicitly model the runoff; rather, meltwater collecting in the lowest grid element is used to saturate the snow, starting with the lowermost grid element and proceeding upward. The thickness of the slush layer is restricted, and the remainder of the meltwater is assumed to run off. The implicit assumption made in this procedure is that the model always extends to the depth of the first impermeable ice layer, and that no other layers form at shallower depths during the simulation. Greuell and Oerlemans (1986) use a simpler model in which meltwater is allowed to penetrate downward until a layer with a density larger than 800 kg/m^3 is reached and the water is assumed to run off.

Wakahama (1968) and Colbeck (1973) suggest that the rate of firn compaction increases when the water saturation is large. Except just above layers of impermeable ice, these conditions normally do not occur, and for high-density, wet snow with almost spherical grains, the rate of increase in density should be similar to that for dry snow (Yen, 1981). For freshly fallen, low-density snow, Yen (1981) argues that the presence of liquid water will accelerate the destructive metamorphism, thereby increasing the settling rate. Refreezing of meltwater may result in the formation of ice layers and lenses, thus providing a rapid mechanism for transforming snow into ice. A general expression for the change in density caused by melting or refreezing has not yet been derived, and most models incorporate the effects of melt-freeze cycles in an ad hoc way. For example,

Greuell and Oerlemans (1986) take the rate of densification to be a function of meltwater such that a melting rate of 2 cm/day increases the densification rate by a factor of about 7. Greuell and Konzelmann (1994) do not include the decrease in density when internal melting occurs because inclusion of this process led to numerical problems. Instead, these authors prescribed an unrealistically low value for the irreducible water amount to reduce the densification rate due to refreezing of meltwater.

6.8 CALCULATED NEAR-SURFACE SNOW TEMPERATURES AT SOUTH POLE STATION

By coupling the calculation of surface fluxes to the thermodynamic equation (6.17), the change in firn temperatures throughout the year or under altered climate conditions can be numerically simulated. As an example, the annual temperature cycle at South Pole Station is considered in this section. The purpose here is not to present the most accurate calculation of englacial temperatures but rather to illustrate the procedure and how model results can be validated against available data. The model used in this section is essentially the same as that used by Van der Veen and Jezek (1993) to study the seasonal firn temperature near Vostok Station.

The temperature equation (6.17) may be simplified by making the usual assumptions that horizontal advection and diffusion of heat may be neglected and that strain heating is small near the surface of the glacier. In an exception to the general convention used in this book, the vertical z-axis is taken positive *downward*, with z = 0 at the surface. The thermodynamic equation then becomes

$$\frac{\partial T}{\partial t} = \frac{\partial}{\partial z} K \frac{\partial T}{\partial z} + w \frac{\partial T}{\partial z} - \frac{1}{\rho C_p} \frac{\partial Q_a}{\partial z}. \tag{6.86}$$

The last term on the right-hand side corresponds to the last term on the right-hand side of equation (6.17) and represents the heat added to a layer at depth z. Neglecting melting and refreezing of meltwater (as is appropriate for central East Antarctica), the only source of heat below the surface is short-wave solar radiation penetrating into the firn as described by equation (6.47). The amount of radiation absorbed in a layer at depth z below the surface is the difference between the radiation entering this layer at the top and exiting at the bottom to deeper layers. Thus,

$$\frac{\partial Q_a}{\partial z} = \beta I_s(h - z), \tag{6.87}$$

with the radiation flux at depth, $I_s(h - z)$, given by equation (6.48).

Near the surface of the glacier, large temperature gradients may develop as the surface is being cooled or heated, while at greater depths, the gradients tend to become smaller and not changing as much throughout the year. This means that

the grid spacing should be small near the surface (a few cm) but the spacing may increase with depth. The calculations discussed here apply to the upper 55 m of firn, and the spacing increases from 8 cm just below the surface, to 12 m between the lowest two model layers. Because of the variable grid spacing, vertical derivatives cannot be simply estimated from central differences. One possibility is to introduce a new coordinate, s = ln(z), and rewriting equation (6.86) in terms of this coordinate. By taking the spacing between adjacent s-layers constant, ds = 0.25, say, the physical layer thickness increases from 8 cm to 12 m over the model domain. Another possibility for calculating vertical derivatives at gridpoint I is to approximate the temperature profile by a third-order polynomial through the three neighboring grid points I – 1, I, and I + 1. Derivatives are then readily estimated from the coefficients of this polynomial. Results for both approaches are practically the same.

To solve equation (6.86) numerically, two boundary conditions are needed. At the lower boundary, the temperature is prescribed at the measured temperature and kept fixed. The surface temperature is calculated explicitly and changes in response to the heat exchange between the surface and the atmosphere, as described by the total energy flux Q_s, and as a result of downward heat conduction to deeper layers. Following Goddard (1975), the downward heat flux is parameterized as

$$Q_d = \frac{K}{d}(T_d - T_s), \tag{6.88}$$

where T_d represents the temperature at depth d below the surface, here taken to be the temperature of the first depth layer.

Vertical advection of heat (the second term on the right-hand side of equation (6.86)) can be estimated by taking the vertical velocity, w, to decrease linearly from the surface to the bed of the glacier. At the surface, w equals the accumulation rate (noting that z increases downward), while at the bed, w is zero. However, accumulation at South Pole is very small, and consequently, vertical advection has little effect on the calculated temperatures. Similarly, the heat flux associated with precipitation is very small and not discussed here.

As input for the model, the air temperature, wind speed, cloudiness, and air pressure need to be prescribed. For these, the multiyear monthly mean values given in Dalrymple (1966) and shown in Figure 6.11 are used, with the understanding that these values are representative for the midmonth climate. To obtain smoothly varying records of climate, these midmonth values are linearly interpolated. Preferably, a more continuous record of, say, daily observations should be used, but such long-term records are scarce.

The thermodynamic equation (6.86) is solved by numerical integration. At the start of the simulation, the model is run until a steady state is reached for the applicable climate (in this case, January 1). To adequately model the annual cycle, several years are simulated to minimize the effect of the initial temperature conditions. Results discussed below pertain to the fifth model year. Because of the small grid spacing near the surface, a small time step (1 minute) must be used to prevent numerical instabilities.

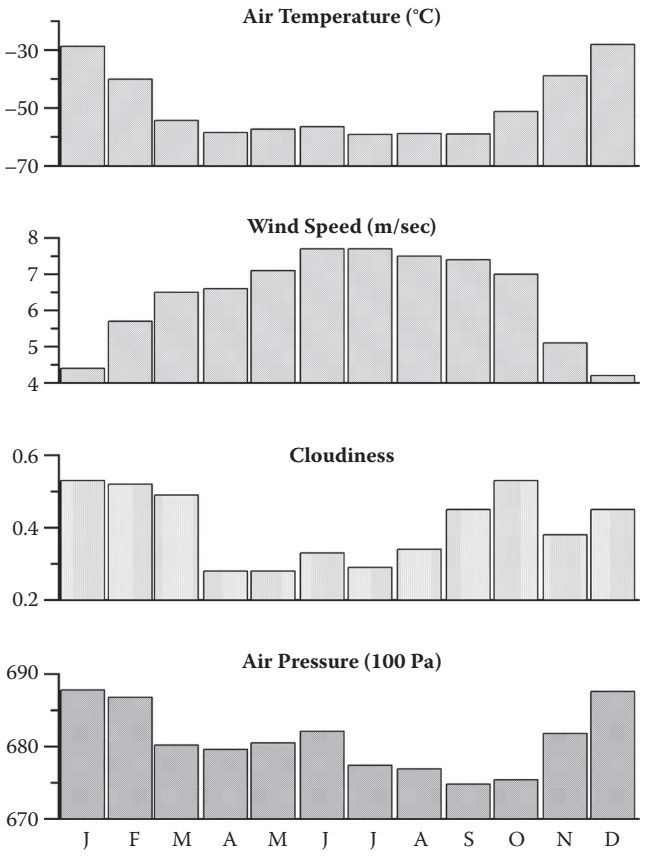

FIGURE 6.11 Monthly mean multiyear meteorological data used as input for the calculation of the firn temperature at South Pole Station. (Based on data from Dalrymple, P. C., in *Studies in Antarctic Meteorology,* American Geophysical Union, Washington, DC, 195–231, 1966.)

Calculated surface fluxes at local noon are shown in Figure 6.12. During the austral winter (mid-March to early September), no solar radiation reaches the surface, and incoming long-wave radiation is small because of the low air temperatures. As a result, the net radiative flux is directed toward the atmosphere, representing loss of heat for the snow surface. During the austral summer, incoming solar and long-wave radiation increase, reversing the direction of the net radiative heat flux. The latent heat flux is small compared with these radiative fluxes. The reason for this is that the air is very dry because of the low temperatures. The sensible heat flux is more important in heating the snow during the austral winter, when the air is slightly warmer than the snow surface (Figure 6.13). During the summer months, when incoming radiation raises the snow temperature above that of the air, the sensible heat flux is directed toward the atmosphere. Finally, heat conduction from the surface to the deeper layers (equation (6.88)) is slightly positive during the winter (indicating that

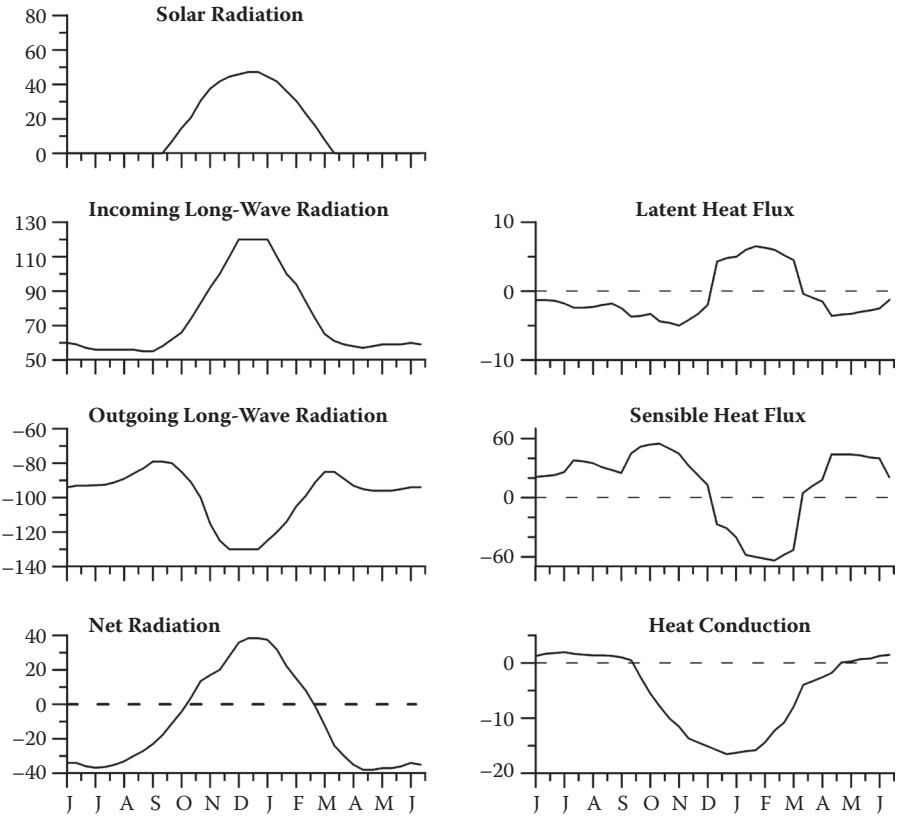

FIGURE 6.12 Calculated surface fluxes (in W/m^2) at solar noon for South Pole. Positive fluxes are directed downward and represent heat gain for the glacier surface. Note the difference in vertical scales for the three panels on the right.

heat is transported upward in the firn because the surface is coldest), but negative during the prolonged summer, when the surface is warmer than the snow below.

The calculated surface temperature agrees within a few degrees with monthly mean surface temperatures measured during the International Geophysical Year, or IGY (1957–1958), as shown in Figure 6.13. The measurements given in Dalrymple (1966) do not include the summer maximum (December–January). The comparison shows that calculated midwinter temperatures are too high. This may be because multiyear averages for the meteorological variables were used in the calculation, whereas the monthly mean surface temperatures shown in Figure 6.13 apply to one year only. In particular, the air temperature, and thus the incoming long-wave radiation and the sensible heat flux, may vary by several degrees from year to year (Schwerdtfeger, 1970), which could easily raise or lower the temperature of the snow surface by a few degrees. Another possibility for the discrepancy between model calculations and measurements is that the model is driven by monthly mean meteorological conditions, which are interpolated to obtain a continuous record. As a result,

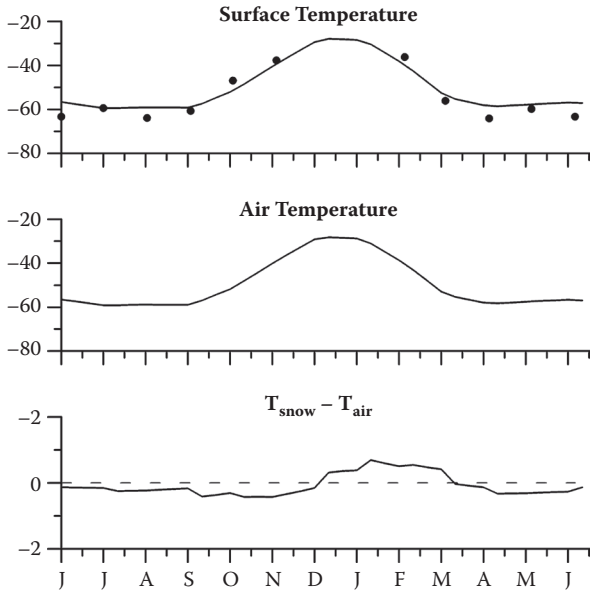

FIGURE 6.13 Comparison between the calculated surface temperature and measured monthly mean values (upper panel; note that the measurements from Dalrymple and others (1966) do not include December and January). The middle panel shows the air temperature (in °C) used as input, and the lower panel shows the calculated difference between the temperature of the glacier surface and the air temperature.

the midwinter minimum in air temperature, as well as the midsummer maximum, are apt to be underestimated. This points to the need of simultaneously obtaining accurate and continuous records of, most importantly, air temperature and wind speed, as well as the snow surface temperature. The calculated temperature of the snow surface represents the most critical model result that can be directly verified against measurements to test the model and especially the parameterizations of the heat exchange between the glacier and atmosphere.

Radiative fluxes can be measured directly and the net monthly mean radiative flux measured at South Pole is shown in Figure 6.14, as well as the monthly mean flux computed by the model (note that the measurements do not cover the months of December and January). Agreement is satisfactory given the uncertainty in measurements (Dalrymple et al., 1966) and the fact that the prescribed air temperature may be different from the actual air temperature during the period of measurements (the IGY), as noted above.

The turbulent fluxes of latent and sensible heat can also be measured directly by means of eddy-covariance sensors. However, this is expensive and requires significant instrument power (D. van As, pers. comm., 2012). Therefore, in most applications, these fluxes are calculated from measured vertical profiles of air temperature and wind speed, by using formulas similar to those given in Section 6.6. Fluxes calculated by Dalrymple et al. (1966) are shown in the lower two panels of Figure 6.14,

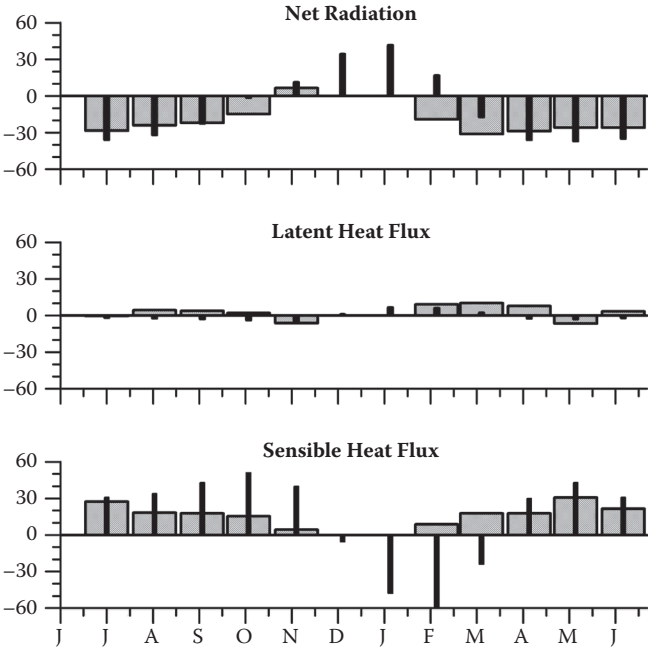

FIGURE 6.14 Comparison between monthly mean surface fluxes (in W/m^2) calculated with the numerical model (black bars) and those inferred by Dalrymple (1966) (hatched boxes).

as well as the monthly mean fluxes calculated by the model. As discussed above, the latent heat flux is small, according to Dalrymple et al. (1966) and to the model. The difference between both estimates for the sensible heat flux is rather large, with the exception of the winter months. This is a disturbing result that most likely can be attributed to the parameterization used, as well as to the air temperature profile. For example, Stearns and Weidner (1993) give estimates for the sensible heat flux that differ substantially from those in Dalrymple et al. (1966).

Calculated englacial temperatures are shown in Figure 6.15. As expected, the annual variation affects only the upper 10 m of the firn (a posteriori justifying the lower boundary condition of fixed temperature). Because the austral winter is of longer duration than the austral summer, the annual cold wave penetrates somewhat deeper than its warm counterpart. The relative warming of the surface during the summer is slightly larger than the relative cooling during the winter. This general pattern agrees well with the firn temperatures measured at South Pole Station during 1957–1958 (Dalrymple, 1966), as shown in Figure 6.16. There are some differences, most notably in the timing of the winter minimum and summer maximum temperatures at depth. This may, however, be very well the result of differences between the actual climate conditions during this period and those prescribed for the model calculations.

The comparison between model results and measured data highlights one of the problems encountered most often, namely, incomplete or nonsimultaneous data sets.

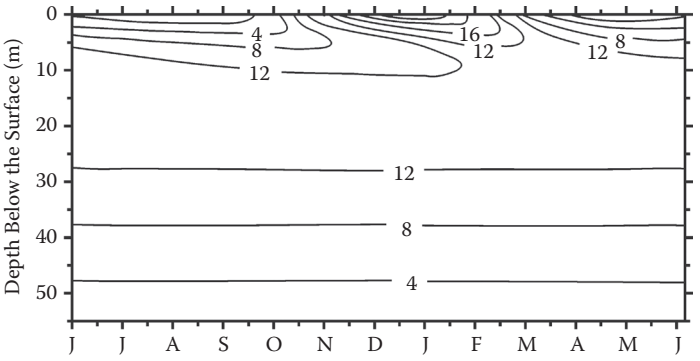

FIGURE 6.15 Calculated annual cycle in temperature at depth for South Pole Station. Contours show the difference between the calculated temperature at depth and the temperature at 66 m depth (kept fixed in the model).

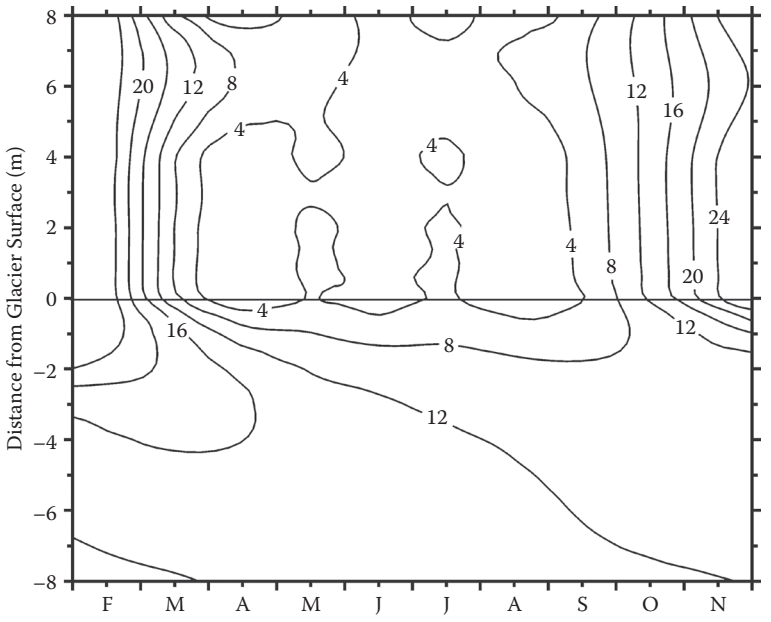

FIGURE 6.16 Temperatures in the firn and atmospheric boundary layer measured at South Pole Station during 1957–1958. To allow for a comparison with Figure 6.15, contours show the difference between the measured temperature and the temperature at 66 m depth. (Based on data from Dalrymple, P. C., in *Studies in Antarctic Meteorology,* American Geophysical Union, Washington, DC, 195–231, 1966.)

The calculations are based on multiyear monthly mean climate meteorological parameters, interpolated to obtain hourly values describing the annual cycle. However, comparable data against which the model results can be tested are not available, but only firn temperatures measured during the course of one year. This particular year may not be indicative of the longer-term climate, given the large variability in air temperatures observed at South Pole Station. To circumvent this problem, simultaneous meteorological observations and measurements in the firn should be conducted. Kuipers Munnike et al. (2009) present measurements of the surface energy balance at Summit, Greenland, and show that measured firn temperatures can be satisfactorily modeled with an energy balance model similar to the one used in this section.

Inspection of the thermodynamic equation (6.86) shows that the temperature at depth is determined by vertical conduction and vertical advection of heat, absorption of solar radiation by deeper layers, and the density-dependency of the thermal diffusivity. In addition, where firn temperatures are close to the melting temperature, meltwater penetration and refreezing may also be important. Greuell and Konzelmann (1994) conducted some sensitivity experiments to determine which of these processes is most important. They conclude that for the location of the ETH Camp, in East Greenland, the largest amount of heating of the upper firn layers is caused by refreezing of downward percolating meltwater. This is probably the least understood process included in their model. The second most important process is absorption of radiation at depth, as confirmed by Kuipers Munnike et al. (2009). The density-dependency of the diffusivity has only a small effect, while other processes in their model do not result in noticeable heating or cooling of the upper layers. Of course, these conclusions cannot be directly applied to other locations, such as central East Antarctica, where surface melting does not occur.